

# Morphology-engineering of ultrathin $\text{In}_2\text{S}_3$ / mesoporous $\text{TiO}_2$ heterojunctions via precursor-directed synthesis for efficient photocatalysis

YU-PEI LI<sup>1,2</sup>, FENG-WEI CHEN<sup>2</sup>, XIAO-JING WANG<sup>2</sup>, BEN-QIAN LU<sup>2</sup>, YA-LI ZHANG<sup>2</sup>, JUN ZHAO<sup>2,3,\*</sup>, YONG-QIANG CHENG<sup>1,\*</sup>, DONG ZHANG<sup>1</sup>

<sup>1</sup>Key Laboratory of Medicinal Chemistry and Molecular Diagnosis, Ministry of Education, Key Laboratory of Analytical Science and Technology of Hebei Province, College of Chemistry and Environmental Science, Hebei University, Baoding, 071002, China

<sup>2</sup>College of Science, Hebei University of Science and Technology, Shijiazhuang, 050018, China

<sup>3</sup>State Key Laboratory of Inorganic Synthesis and Preparative Chemistry, International Joint Research Laboratory of Nano-Micro Architecture Chemistry, College of Chemistry, Jilin University, Changchun, 130012, China

Synthesis of nanostructured materials with unique composition, size and morphology plays a crucial role in designing high-efficient photocatalysts. In this work, a novel precursor-directed synthetic route is developed to construct ultrathin  $\text{In}_2\text{S}_3$ /mesoporous  $\text{TiO}_2$  heterojunction by in situ decorating  $\text{TiO}_2$  on the surface of ultrathin  $\text{In}_2\text{S}_3$  nanoflakes. The solid-state titanium alkoxide is an important precursor, which can be converted directly to porous  $\text{TiO}_2$  for increasing the specific surface area of  $\text{TiO}_2$ . Meanwhile, the ultrathin  $\text{In}_2\text{S}_3$  nanoflakes are in situ constructed via precursor-directed synthetic process with the thickness less than 3nm, which can supply numerous specific surface areas and a large number of active sites for the nucleation of  $\text{TiO}_2$  during the hydrothermal synthesis and result in the uniformly dispersed  $\text{TiO}_2$  nanoparticles. The results confirm that the constructed  $\text{In}_2\text{S}_3/\text{TiO}_2$  heterojunction possesses high specific surface area up to 139.72  $\text{m}^2/\text{g}$ . More importantly, the employment of unique synthetic method together with heterostructure design not only broaden the light absorption of catalyst to visible light region but also create tight interface bonding between  $\text{In}_2\text{S}_3$  and  $\text{TiO}_2$  to achieve higher efficiency in charge transfer and separation. Thus, the obtained catalysts exhibit outstanding photoactivity for methyl orange (MO) degradation with visible light irradiation. This current work presents a simple and effective avenue for constructing nanomaterials with morphology control, which may be promising for rational design of solar conversion and storage devices.

(Received May 31, 2021; accepted June 7, 2022)

**Keywords:** Nanostructured materials, Precursor-directed,  $\text{In}_2\text{S}_3/\text{TiO}_2$  heterojunction, Solid-state titanium alkoxide, Methyl orange (MO) degradation

## 1. Introduction

The semiconductor photocatalysis via sunlight-induced photoredox reactions has attracted

extensively attention due to its potentiality for addressing the global environmental and energy problems [1, 2]. Among various studies in solar energy conversion, rational design and facile synthesis of photocatalytic

nanomaterials plays an increasingly important role [3–5]. Since the discovery of photoelectrochemical (PEC) water splitting reported by Fujishima in 1972, TiO<sub>2</sub> has been researched extensively as a promising semiconductor photocatalyst [6]. However, the practical utilization of TiO<sub>2</sub> is still severely limited by the poor absorption of solar energy because of the wide energy band gap (about 3.2 eV) [7–11]. Besides, the fast recombination of photogenerated carriers and sluggish charge transfer efficiency also affect its photocatalytic activity [12–14]. To date, continuous attempts have been devoted to solving these issues by enhancing the optical absorption and charge transfer properties of TiO<sub>2</sub>, such as morphology control [15–17], chemical doping [18–20], energy band modulation [21–23] and the construction of heterojunctions [24–27]. In particular, the simultaneously realized heterojunction design together with morphology control not only enable the photocatalysts possess better light absorbance but also achieve an effective separation of charge pairs and subsequent transfer across the interface more efficiently.

In recent years, indium sulfide (In<sub>2</sub>S<sub>3</sub>) nanomaterial has garnered extensive interest ascribed to its narrow band gap (1.9 eV~2.2 eV) that can make full use of solar energy from visible light to near-infrared (NIR) light. In<sub>2</sub>S<sub>3</sub> is always used as the visible-light-driven catalyst and usually coupled with wide band-gap semiconductors to construct heterojunction structures [28–30]. Among them, In<sub>2</sub>S<sub>3</sub>/TiO<sub>2</sub> heterojunction is one of the most widely studied structures. In<sub>2</sub>S<sub>3</sub> and TiO<sub>2</sub> have suitable band levels that match well with each other and a built-in electrical field would form due to the intimate contacts between two semiconductors, which are beneficial to enhancing the charge separation and transfer and then the subsequent photocatalytic activity [31–35]. For examples, In<sub>2</sub>S<sub>3</sub>/TiO<sub>2</sub> composite with broadened absorption range has been prepared by a facial chemical precipitation method reported by Huang's group [34]. In the following year, Chai et al. successfully fabricated the In<sub>2</sub>S<sub>3</sub>/(Pt-TiO<sub>2</sub>) nanocomposite containing floriated In<sub>2</sub>S<sub>3</sub> and TiO<sub>2</sub> nanoparticles via multi-step method [35]. Benefiting from the efficient transfer of photogenerated charge carriers from In<sub>2</sub>S<sub>3</sub> to TiO<sub>2</sub>, the obtained catalyst exhibited remarkably improved photocatalytic activity.

Very recently, Wang and co-authors investigated the PEC properties of various In<sub>2</sub>S<sub>3</sub> nanostructures. They found that TiO<sub>2</sub>/In<sub>2</sub>S<sub>3</sub> photocatalysts with wedged structure exhibited enhanced light absorption ability and thus excellent PEC performance [36]. Nonetheless, the constructed In<sub>2</sub>S<sub>3</sub>/TiO<sub>2</sub> composites in the previous reports usually need pre-prepared TiO<sub>2</sub> with high-temperature treatment for subsequently reacting with indium source during the synthetic procedure, which is prejudicial to further structural engineering at molecular-level. Hence, it is relatively meaningful to develop novel synthetic strategy for in situ fabricated In<sub>2</sub>S<sub>3</sub>/TiO<sub>2</sub> heterojunctions at low temperature together with morphology control.

The precursor-directed synthetic strategy has been proven as an efficient approach to guide nanomaterials in well-controlled shapes, structures and compositions [37]. Metal alkoxides, benefitting from the synergistic effects of their inorganic and organic components, have been widely used as unique precursor materials for the preparation of nanostructured functional materials [38, 39]. For example, Zhao's group reported the synthesis of porous TiO<sub>2</sub> microspheres that were composed of {010}-faceted nanobelts using titanium glycerolate as precursor during the simple hydrothermal treatment [40]. Due to the enlarged surface area and high exposure of {010} facets, the synthesized TiO<sub>2</sub> photocatalyst displayed highly enhanced photocatalytic activity in H<sub>2</sub> evolution, which was more than twice higher compared to P25. Inspired by this research, we can predict that a hydrothermal-based approach could be adopted to controllably prepare semiconductor heterojunctions and simultaneously realize morphology control using metal alkoxides as precursor.

In this work, we present a novel precursor-directed solvothermal method to in situ construct heterojunctions consisting of In<sub>2</sub>S<sub>3</sub> nanoflakes and TiO<sub>2</sub> nanoparticles using solid-state metal alkoxide as precursor. The In<sub>2</sub>S<sub>3</sub> nanoflakes act as sensitizer and will generate electron-hole pairs under visible light irradiation and TiO<sub>2</sub> will accept electrons to reduce the recombination of the charge carriers simultaneously. Thus, the obtained In<sub>2</sub>S<sub>3</sub>/TiO<sub>2</sub> heterojunction exhibits ultrahigh photocatalytic ability for methyl orange (MO) degradation under visible light irradiation. What's more,

the structural properties and photocatalytic mechanism were investigated in detail.

## 2. Experimental section

### 2.1. Materials

Tetrabutyl titanate (TBT) and indium nitrate were supplied by Aladdin Reagents Co., Ltd (Shanghai, China). Isopropanol (IPA) and glycerol were received from Yong Da Chemical Reagent Co., Ltd (Tianjin, China). Thioacetamide (TAA) was supplied by Sinopharm Chemical Reagent Co., Ltd (Shanghai, China). P25 was commercial  $\text{TiO}_2$  powder from Degussa Chemical Co., Ltd (Qingdao, China). All chemicals were analytical grade and directly used as obtained. Deionized water was prepared and throughout used all experiment.

### 2.2. Preparation of catalysts

The synthetic process of ultrathin  $\text{In}_2\text{S}_3$ /mesoporous  $\text{TiO}_2$  heterojunctions is schematically depicted in Fig. 1 via precursor-directed solvothermal method. The precursor of  $\text{TiO}_2$  was synthesized using tetrabutyl titanate as titanium source by a simple solvothermal method. In detail, 1 mL tetrabutyl titanate was dispersed in 20 mL mixture solvent with the volume ratio of glycerol and isopropanol being 1:3. After magnetically stirring for 15 min to a uniform solution, the mixture was

transferred into Teflon-lined autoclave and treated at solvothermal conditions at 180 °C for 16 h. At last, the resulting powders were collected, thoroughly washed and dried at 60 °C in vacuum oven. The component of as-obtained precursors was  $\text{Ti}(\text{C}_3\text{H}_5\text{O}_3)_4$ .

The  $\text{In}_2\text{S}_3/\text{TiO}_2$  heterojunction photocatalysts were synthesized via the similar solvothermal process. Typically, 0.35 g thioacetamide and 0.3 g  $\text{Ti}(\text{C}_3\text{H}_5\text{O}_3)_4$  precursors were fully blended in 45 mL deionized water under magnetic stirring for 30 min. A certain amount of indium nitrate with the calculated In/Ti atomic ratio (1:5, 2:5, 3:5) was subsequently added into the above mixture solution. After continuously stirred for 2 h, the obtained mixture was transferred into Teflon-lined autoclave for hydrothermal reaction at 180 °C for 6 h. Then, the resulting brown precipitates were obtained and collected by centrifugation, thoroughly washed several times and vacuum dried in an oven at 60 °C. The finally obtained samples were denoted as TS-1, TS-2, and TS-3, respectively. For comparison,  $\text{TiO}_2$  nanoparticles were synthesized adopting the similar procedures in the absence of thioacetamide and indium nitrate;  $\text{In}_2\text{S}_3$  nanoflakes were prepared without adding  $\text{Ti}(\text{C}_3\text{H}_5\text{O}_3)_4$  precursors into the reaction solution and named as  $\text{In}_2\text{S}_3$ ; The  $\text{In}_2\text{S}_3/\text{P25}$  heterojunctions were synthesized by just replacing  $\text{Ti}(\text{C}_3\text{H}_5\text{O}_3)_4$  precursor as P25 and the as-obtained samples were named as  $\text{P}_{25}\text{S-2}$ , which is reference to the amount of TS-2.

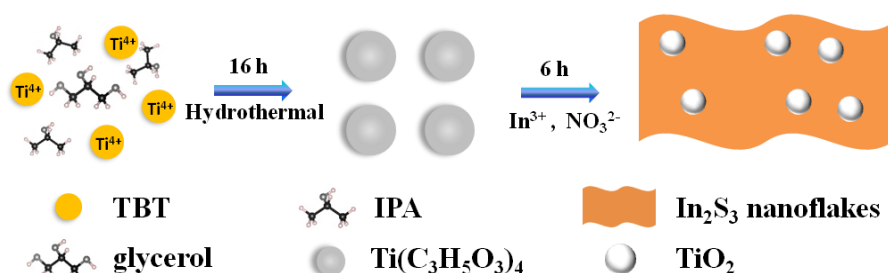


Fig. 1. Schematic illustration of precursor-directed solvothermal method to in situ construct ultrathin  $\text{In}_2\text{S}_3$ /mesoporous  $\text{TiO}_2$  heterojunctions (color online)

### 2.3. Characterization measurement

X-ray diffraction (XRD, Bruker D8) data were measured to analyze the composition of samples. The

scanning electron microscopy (SEM; Hitachi S-4800) images were obtained to observe the morphological features of samples. The transmission electron microscopy (TEM; JEOL JEM-2100) were used to

survey the microstructure of the catalysts. The nitrogen adsorption and desorption curves and porous distribution were completed using the Micromeritics Tristar II 3020 apparatus. X-ray photoelectron spectroscopy (XPS, PHI 1600 ESCA) analysis were carried out to investigate the surface chemical states of the samples and the valence band spectra. Diffuse reflectance spectroscopy (DRS, Thermo Fisher Evolution 220) was performed over the range of 200–800 nm. The photoluminescence (PL) spectra of the samples were recorded at room temperature on a Hitachi F-4600 fluorescence spectrophotometer excited by a 340 nm incident light.

Electrochemical tests were conducted on a CHI660E electrochemical analyzer (Chenhua, Shanghai), using platinum electrode as the counter electrode and Ag/AgCl electrode as the reference electrode, respectively. Na<sub>2</sub>SO<sub>4</sub> solution (0.2 M) was used as an electrolyte. In a typical procedure, the working electrode was prepared as follows: a certain amount of catalyst powders were dispersed into a mixture (30  $\mu$ L of 5% Nafion solution, 240  $\mu$ L glycols, and 720  $\mu$ L deionized water) under ultrasonically treatment. The obtained slurry was spread on a prepared FTO glass electrode with a tailored size of 1.0 cm $\times$ 1.0 cm.

#### 2.4. Test of photocatalytic activity

Photocatalytic degradation tests were conducted using MO as the target pollutant. A xenon arc lamp (PLS-SXE300D, 300 W) was used as the light source equipped with 400 nm cut-off filter. The distance from Xe lamp to reactant solution was controlled at 20 cm and the measured light intensity was 100 mW/cm. Typically, a given amount of catalyst powders were dispersed into 10 mg/L MO solution and then magnetically stirred for 30 min in a darkroom for adsorption/desorption equilibrium. Then mixture was irradiated by Xe lamp with visible light. 4 mL suspensions were collected and separated by centrifugation at certain time intervals. The concentration of MO was determined by UV-vis spectrophotometer at 464 nm. In order to investigate the stability of photocatalyst, the durability test of catalysts was also carried out as follows: after photocatalytic reaction, the catalyst was withdrawn from solution by

centrifugation at 10000 rpm, then reused for the next round experiment after drying at 60  $^{\circ}$ C under vacuum.

### 3. Results and discussions

#### 3.1. Structure and morphology characterization

Powder XRD were firstly investigated to determine the crystalline degree and phase composition of as-synthesized photocatalysts. As shown in Fig. 2, the pure TiO<sub>2</sub> samples are well indexed to anatase crystalline phase according to the JCPDS card No. 21-1272. The strongest diffraction peak at 25.3  $^{\circ}$  indicates that the major exposed plane of TiO<sub>2</sub> is the (101) facet [41]. As for In<sub>2</sub>S<sub>3</sub>, the crystalline reflections in XRD patterns at 27.4  $^{\circ}$ , 33.2  $^{\circ}$  and 47.7  $^{\circ}$  correspond to the (109), (0012), (2212) planes by careful comparison with the standard pattern (JCPDS No. 25-0390), indicating the formation of  $\beta$ -In<sub>2</sub>S<sub>3</sub> structure and the high purity of prepared In<sub>2</sub>S<sub>3</sub> [42]. Comparatively, the XRD patterns of the In<sub>2</sub>S<sub>3</sub>/TiO<sub>2</sub> heterojunctions seem to be superimposition of pattern TiO<sub>2</sub> and In<sub>2</sub>S<sub>3</sub>. Furthermore, the gradual increase in characterized diffraction peaks intensity of In<sub>2</sub>S<sub>3</sub> suggests the increasing amount of In<sub>2</sub>S<sub>3</sub> nanoflakes coupling with TiO<sub>2</sub> nanoparticles. These results also indicate that the successfully construction of In<sub>2</sub>S<sub>3</sub>/TiO<sub>2</sub> heterojunctions. Besides, the considerably weaker intensity and broader peak width in XRD patterns are probably induced by the small size effect and relatively weak crystalline nature of photocatalysts.

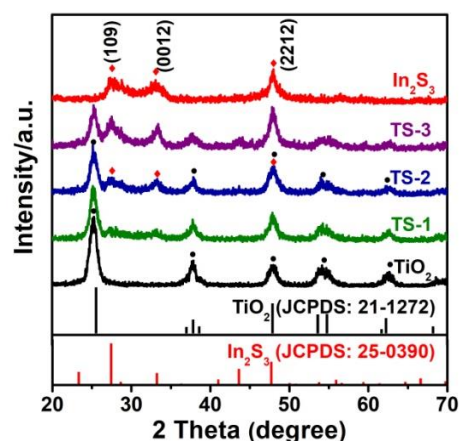


Fig. 2. XRD patterns of In<sub>2</sub>S<sub>3</sub>/TiO<sub>2</sub> heterojunctions (color online)

The SEM images were used to probe the morphology of as-synthesized samples. As shown in Fig. 3a, pure  $\text{TiO}_2$  exhibits a irregular granuliform-like surface morphology. Comparatively, for pure  $\text{In}_2\text{S}_3$  presented in Fig. 3b, it is composed of lamellar-like structure with interconnected ultrathin nanosheets, which randomly arrange together to form hierarchical structure. When  $\text{In}_2\text{S}_3/\text{TiO}_2$  heterojunction is compounded (Fig. 3c and d), the size of composite becomes comparatively uniformly and the particle size decreases drastically. So we can

speculate that  $\text{TiO}_2$  nanoparticles firstly adhere to the surface of  $\text{In}_2\text{S}_3$  nanoflakes and then the samples assemble together to form bigger particles. It can be clearly observed from the magnified image (Fig. 3d inset) that the  $\text{In}_2\text{S}_3/\text{TiO}_2$  heterojunctions are composed of irregular nanoparticles and a large number of tiny flakes, which could offer more accessible channels and catalytic sites for reactant transfer and reactivity in photocatalytic process [28].

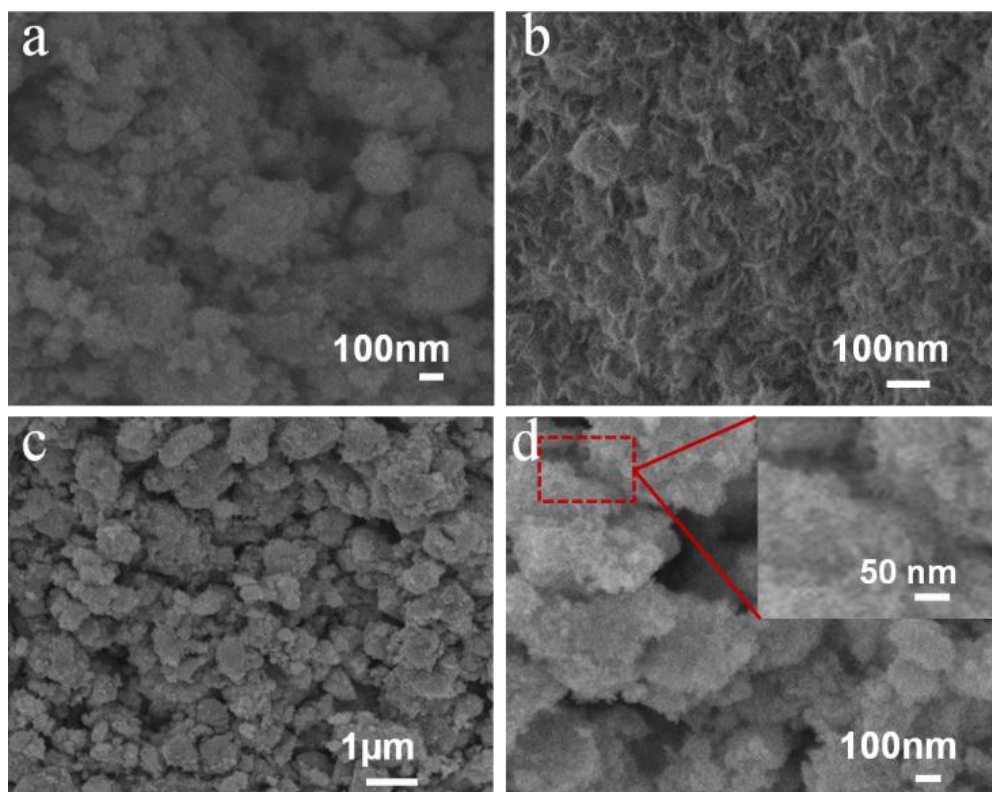


Fig. 3. SEM images of samples: (a)  $\text{TiO}_2$ ; (b)  $\text{In}_2\text{S}_3$ ; (c) and (d) TS-2 (color online)

The detailed microstructures and crystal phases of as-synthesized catalysts were further analyzed by TEM images and shown in Fig. 4. Apparently, the pure  $\text{TiO}_2$  samples exhibit irregular nanoparticle structure with the size around 10 nm (Fig. 4a). As for TS-2 (shown in Fig. 4b and c), the curly and wrinkled structures clearly indicate the ultrathin structure of  $\text{In}_2\text{S}_3$  nanoflakes, which can supply larger specific surface areas and numerous active sites for the nucleation of  $\text{TiO}_2$  during the hydrothermal synthesis of heterostructures and result in the uniformly dispersed  $\text{TiO}_2$  nanoparticles. In addition, the TEM images of TS-2 in Fig. 4b clearly exhibit the

thickness of most nanoflakes being less than 3.0 nm. Moreover, the correspondingly SAED pattern of  $\text{TiO}_2$  and  $\text{In}_2\text{S}_3/\text{TiO}_2$  heterojunctions shown in the inset picture in Fig. 4a and b was further measured to probe the crystalline and composition nature of  $\text{TiO}_2$  and  $\text{In}_2\text{S}_3$ . The main lattice distance in Fig. 4a is 0.35 nm for (101) plane of  $\text{TiO}_2$ . After coupling with  $\text{In}_2\text{S}_3$ , extra lattice distances could be detected with 0.19 nm for (2212) and 0.32 nm for (109) planes of  $\text{In}_2\text{S}_3$ , respectively. The HRTEM images show observable interfaces between two phases in the heterojunctions. As can be seen from Fig. 4d, the largest portion with the 0.35 nm lattice fringes is ascribed

to (109) planes of  $\text{TiO}_2$  nanoparticles and the 0.32 nm lattice fringes is ascribed to (109) planes of  $\text{In}_2\text{S}_3$ , which

further demonstrates the formation of heterojunction structure.

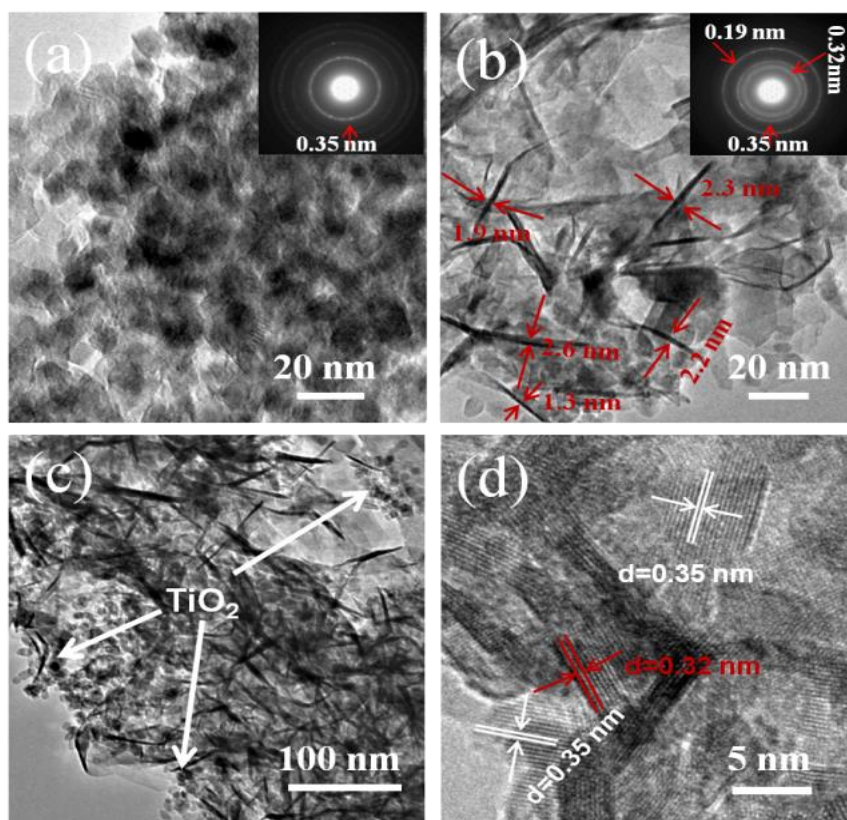


Fig. 4. TEM images of (a)  $\text{TiO}_2$ ; (b), (c) TS-2; and (d) HRTEM image of TS-2 (color online)

The nitrogen adsorption-desorption isotherms and the corresponding pore size distribution curve were used to explore the specific surface area and porous structure of as-obtained samples and shown in Fig. 5. According to the IUPAC classifications, all isotherms are identified as typical type II-like curves with H3 hysteresis loop, which indicates the existence of lamellar stacking of nanoflakes [43]. The distribution curves of pore size (inset in Fig. 5) were obtained ranging from 3 to 40 nm using the BJH method from the desorption branch of the isotherm. Hence, the calculated BET specific surface area ( $S_{\text{BET}}$ ) and the pore parameters of all the samples are listed in Table 1. Compared with P25 and  $\text{In}_2\text{S}_3$ , the precursor-directed fabricated samples possess higher specific surface areas of  $156.82 \text{ m}^2/\text{g}$  for  $\text{TiO}_2$ , and  $139.72 \text{ m}^2/\text{g}$  for TS-2, respectively, indicating the significance of precursor in the synthetic process, which could supply more catalytic active sites and result in improved catalytic activity.

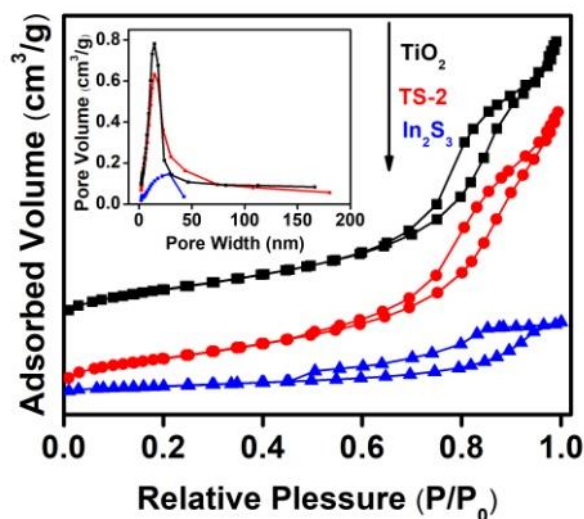


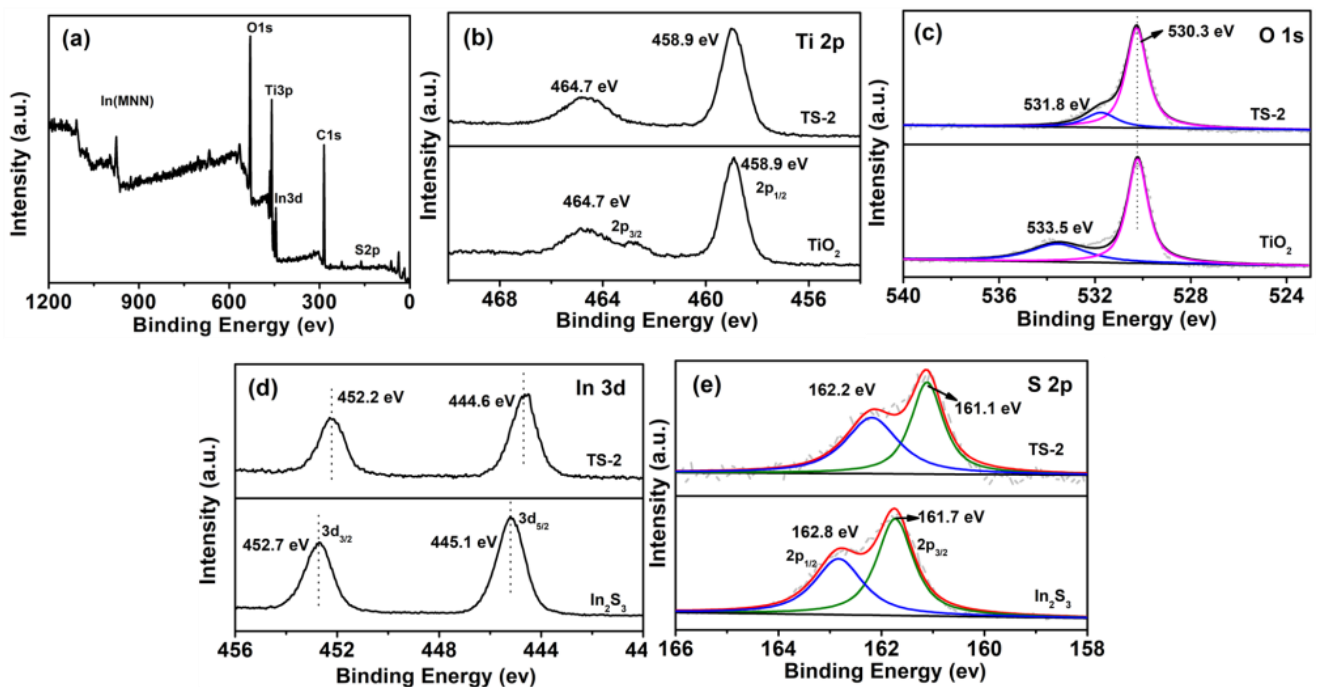
Fig. 5. Nitrogen adsorption-desorption isotherms and the corresponding pore size distribution curves (inset) for the as-synthesized samples (color online)

Table 1. Specific surface areas and pore parameters of the as-prepared samples

Sample I(f)	$S_{\text{BET}}$ ( $\text{m}^2\text{g}^{-1}$ )	Pore volume ( $\text{cm}^3\text{g}^{-1}$ )	Average pore width (nm)
P25	52.10	—	—
$\text{TiO}_2$	156.82	0.48	9.27
TS-2	139.72	0.47	9.74
$\text{In}_2\text{S}_3$	35.41	0.12	9.98

To further analyze the existence of  $\text{In}_2\text{S}_3$  and  $\text{TiO}_2$ , both the chemical compositions and surface oxidation states of  $\text{TiO}_2$  and TS-2 hybrid were assessed using XPS, as shown in Fig. 6. Fig. 6a shows the fully scanned spectrum of TS-2, which reveals the existence of five elements in composite: Ti, O, In, S and C. The observed C signal at 284.6 eV comes from adventitious carbon-based contaminant, which is used to calibrate all of the binding energies [44]. It can be seen that the In and S peaks of the TS-2 hybrid are relatively lower in comparison with Ti and O peaks, which indicates that the TS-2 hybrid contains a small amount of  $\text{In}_2\text{S}_3$ . With regard to the Ti 2p XPS spectra (shown in Fig. 6b), two peaks observed at 458.9 and 464.7 eV for  $\text{TiO}_2$  and TS-2 samples are associated core lines of Ti 2p<sub>1/2</sub> and 2p<sub>3/2</sub>, respectively. Apparently, there is no shift for the two peaks, implying that no conspicuous influence on the energy spectrum of Ti species could be observed by coupling with  $\text{In}_2\text{S}_3$ . The high-resolution spectrum of O

1s in Fig. 6c can be deconvoluted into two peaks at nearly 530.3 and 531.8 or 533.5 eV, corresponding to the metal–oxygen bonds (Ti–O–Ti) in  $\text{TiO}_2$  and O–H bonds on the surface of samples or absorbed  $\text{H}_2\text{O}$ , respectively [45]. From Fig. 6d, the binding energies of In 3d located at 445.1 eV and 452.7 eV in pure  $\text{In}_2\text{S}_3$  could be assigned to In 3d<sub>5/2</sub> and In 3d<sub>3/2</sub>, respectively, indicating the existence of In(III) [46]. As for the TS-2 hybrid, the locations of In 3d peaks in shift to lower binding energy centered at 444.6 eV and 452.2 eV due to the additional coulombic interaction between the emitted electron and the indium core. What's more, with respect to the high-resolution XPS spectra of S 2p (Fig. 6e), doublet peaks located at 161.7 eV for 2p<sub>3/2</sub> and 162.8 eV for 2p<sub>1/2</sub> are deconvoluted in  $\text{In}_2\text{S}_3$ . However, there are obvious shifts for the S 2p<sub>3/2</sub> and S 2p<sub>1/2</sub> peaks in TS-2. Such shifts can be attributed to the chemical interaction between  $\text{In}_2\text{S}_3$  and  $\text{TiO}_2$ , rather than a simple physical contact.

Fig. 6. X-ray photoelectron spectra for  $\text{TiO}_2$ ,  $\text{In}_2\text{S}_3$  and TS-2: (a) survey, (b) Ti 2p, (c) O 1s, (d) In 3d, (e) S 2p (color online)

### 3.2. Optical absorptive ability

The optical absorption properties of TiO<sub>2</sub>, TS-2 and In<sub>2</sub>S<sub>3</sub> were characterized by UV-vis diffuse reflectance spectra. As shown in Fig. 7a, all the samples present distinctly different absorbance and absorption edges. It is seen that TiO<sub>2</sub> can only absorb ultraviolet light region with a dominant absorption edge at about 400 nm. In contrast, In<sub>2</sub>S<sub>3</sub> and TS-2 exhibit obvious red-shifts to visible light absorption region and strong absorption region up to around 650 nm, which could be directly visualized by the color changes (inset in Fig. 7a). Moreover, the corresponding E<sub>g</sub> of TiO<sub>2</sub> and In<sub>2</sub>S<sub>3</sub> are estimated as follows [47, 48]:

$$\alpha h\nu = A(h\nu - E_g)^2 \quad (1)$$

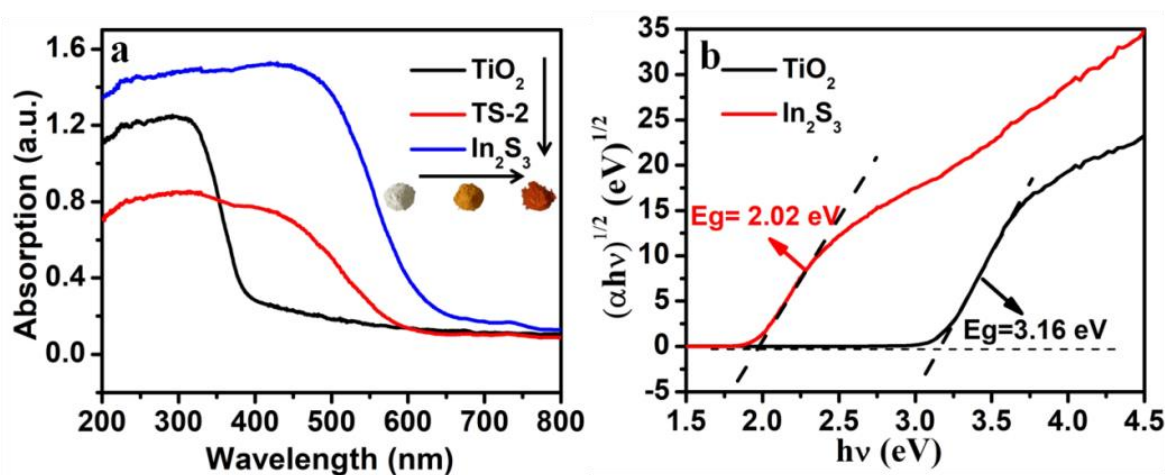


Fig. 7. (a) UV-vis diffuse reflectance spectra of TiO<sub>2</sub>, TS-2 and In<sub>2</sub>S<sub>3</sub> samples; and (b) Plots of  $(\alpha h\nu)^{1/2}$  versus photon energy  $(h\nu)$  for the band-gap energy of TiO<sub>2</sub> and In<sub>2</sub>S<sub>3</sub> (color online)

### 3.3. Charge separation and transfer via heterojunction interfaces

Generally, the charge transfer and separation are important factors for photocatalytic activity. Thus, the separation behavior and transfer efficiency of photogenerated electron/hole pairs were further detected by photoluminescence emission spectra and transient photocurrent response tests (shown in Fig. 8). Fig. 8a shows photoluminescence emission spectra of pure TiO<sub>2</sub> and TS-2. Clearly, the PL spectra of both pure TiO<sub>2</sub> and TS-2 show a main emission peak at about 380 nm, while TS-2 presents a sharply decreased trend. It can also be

From the equation, the corresponding parameters of  $\alpha$ ,  $\nu$ , and  $h$  represent the absorbance, frequency, Planck's constant, respectively.  $A$  is a constant. The value of 2 adopted here is representative for indirect transition semiconductor. So the E<sub>g</sub> of materials could be estimated using Tauc plots of  $(\alpha h\nu)^{1/2}$  versus energy  $(h\nu)$ . As presented in Fig. 7b, the E<sub>g</sub> of TiO<sub>2</sub> and In<sub>2</sub>S<sub>3</sub> obtained from the tangent intercept are 3.16 and 2.02 eV, respectively, which are well consistent with the previous reports [49].

observed that the pure TiO<sub>2</sub> had the maximum emission intensity value and significantly decreased with the modification of In<sub>2</sub>S<sub>3</sub>, nevertheless, TS-2 had lower optical absorption at the excitation wavelength (Fig. 7a). Generally speaking, the higher recombination of charges gives rise to the PL emission signal enhancement under similar light absorption intensity. In other words, lower PL intensity indicates a lower photogenerated charges recombination rate. Therefore, we can infer that the recombination of photogenerated carriers in TiO<sub>2</sub> has been effectively inhibited after the introduction of In<sub>2</sub>S<sub>3</sub>. In order to qualitatively investigate the transfer and separation efficiency of charge  $e^-/h^+$  pairs during the

photoreactions, photocurrent response was measured on electrochemical workstation. As shown in Fig. 8b, the transient photocurrent-time (I-t) curves were obtained by recycling experiment in on-off light illumination. Clearly, after 5 turns of intermittent light switching, the sharp rise and fall of the photocurrent is consistent well with the light on and off cycles, and the photocurrent signal intensity keeps almost unchanged during the photoreaction process, indicating the good stability of prepared samples. It is can be seen that the  $\text{In}_2\text{S}_3/\text{TiO}_2$  heterojunction shows highly enhanced photocurrent than

pure  $\text{TiO}_2$ , which suggests that the  $\text{In}_2\text{S}_3/\text{TiO}_2$  photocatalysts have superior efficiency in separating charge pairs and better interfacial charge transfer. Thus, from the above analysis, we can deduce that the efficient interfacial contact is successfully constructed during the hydrothermal process. This tight contact design is desirable to supply more charge transfer channels between  $\text{TiO}_2$  nanoparticles and  $\text{In}_2\text{S}_3$  nanoflakes for efficiently reducing the recombination of  $e^-/h^+$  pairs in the process of photochemical reaction, which is accordance with the results of TEM image.

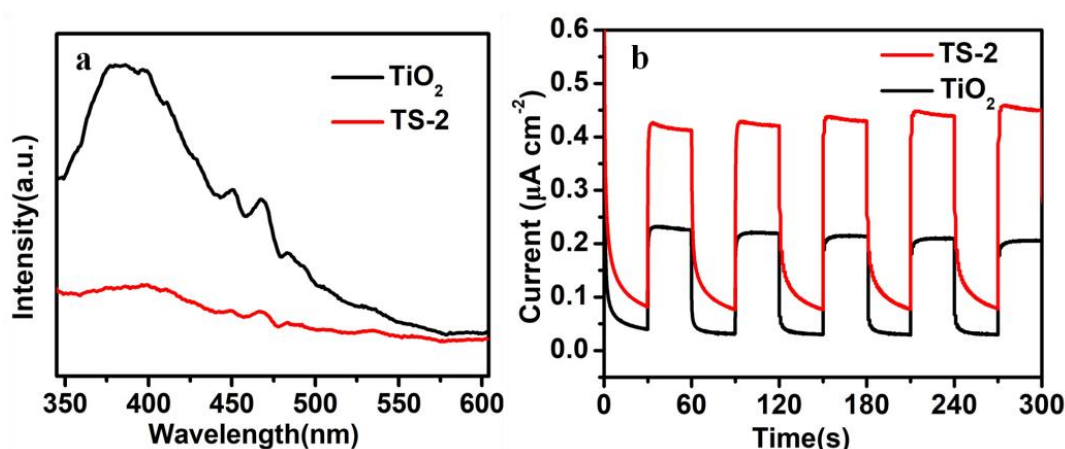


Fig. 8. (a) Steady-state photoluminescence emission spectra and (b) Transient photocurrent responses with light on-off cycles of as synthesized  $\text{TiO}_2$  and TS-2 hybrid (color online)

### 3.4. Photocatalytic activity

The photocatalytic activity of the catalysts was evaluated by degradation of dye molecules (MO) under visible light and simulative solar irradiation, as shown in Fig. 9. Under the same experimental conditions, the self-degradation of MO is nearly negligible as there is only less than 2% degradation rate appearing for MO in the absence of photocatalysts. After light irradiation, it can be found that the  $\text{In}_2\text{S}_3/\text{TiO}_2$  heterojunctions exhibit excellent photocatalytic performances, and the TS-2 catalyst displays the highest degradation rate and almost 90 % of MO is degraded over the TS-2 composite under visible light and simulative solar irradiation in 10 min and 5 min, respectively (Fig. 9a and c). In addition, it is worth to notice that  $\text{TiO}_2$  shows almost negligible photocatalytic activity on MO degradation by visible

light irradiation (Fig. 9a), while remarkably enhanced photocatalytic degradation of MO can be observed under simulative solar irradiation due to its light response only to ultraviolet light (Fig. 9c). The MO photodegradation kinetics on catalysts is evaluated by the reaction rate constant based on the following pseudo-first-order kinetics model [50]:

$$\ln C_0/C_t = kt + \ln C_0/C_1 \quad (2)$$

where  $C_0$ ,  $C_1$  and  $C_t$  stand for the original concentration, the concentration before photocatalytic reaction, and the reactant concentration at certain photocatalytic reaction time, respectively. The parameter  $k$  ( $\text{min}^{-1}$ ) is the pseudo-first-order rate constant. In general, the higher  $k$  value indicates faster reaction rate. The apparent rate constants are obtained from the fitted curves coerced

across the intercepts of  $\ln(C_0/C_1)$  in the y axis (shown in Fig. 8c, d). The calculated  $k$  value of TS-2 is  $0.12719 \text{ min}^{-1}$  in visible light irradiation and  $0.32877 \text{ min}^{-1}$  in solar irradiation, respectively, indicating a significant improvement of photocatalytic ability over TS-2 sample. To further study the effect of specific surface areas and the function of in-situ construction of  $\text{In}_2\text{S}_3/\text{TiO}_2$  heterojunction on photocatalytic performance,  $\text{In}_2\text{S}_3/\text{P25}$  ( $\text{P}_{25}\text{S-2}$ ) hybrid was prepared under the same conditions. As shown in Fig. 10a, the degradation efficiency of TS-2 is over 90% within 10 min visible light irradiation, which is 1.5 times higher compared to  $\text{P}_{25}\text{S-2}$  sample. The

results may attribute to the in-situ constructed nano-junctions at the interfaces between  $\text{In}_2\text{S}_3$  nanoflakes and  $\text{TiO}_2$  nanoparticles as well as the large specific surface areas of  $\text{TiO}_2$ , providing more chances to build ideal interfaces and more active sites and promoting the charge migration across the interfaces more efficiently. The stability study of the  $\text{In}_2\text{S}_3/\text{TiO}_2$  heterojunction was also adopted by recycling the TS-2 sample for degrading MO. From Fig. 10b, a slight loss of photocatalytic activity could be observed after five cycles, which suggests that the in situ constructed  $\text{In}_2\text{S}_3/\text{TiO}_2$  heterojunctions are stable.

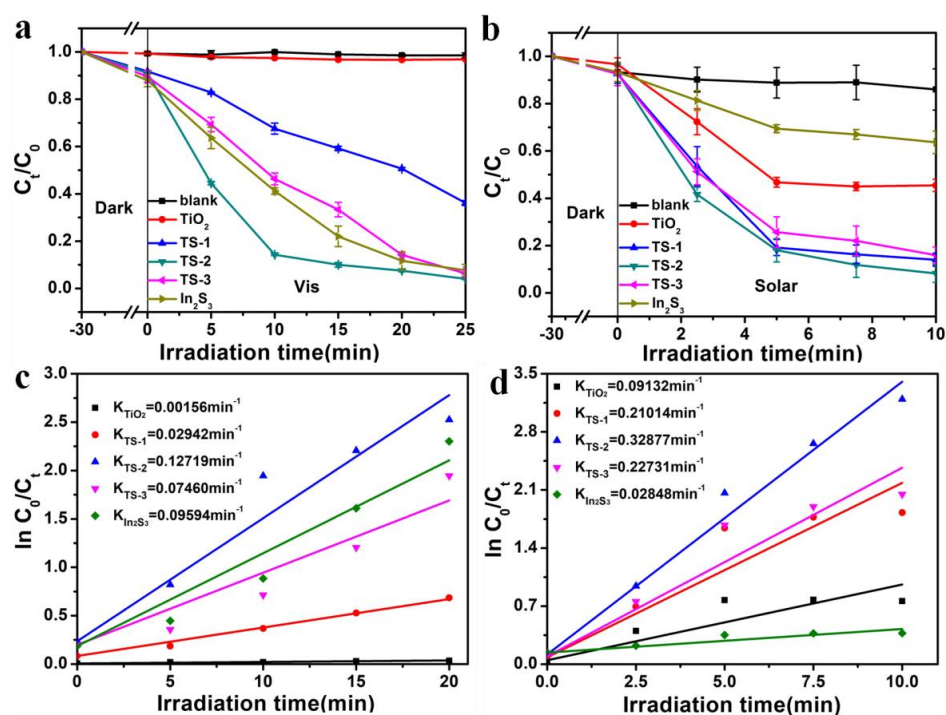


Fig. 9. MO degradation pattern of as-synthesized samples under (a) visible light, (b) simulative solar irradiation; (c) and (d) the corresponding first-order kinetic degradation curve (color online)

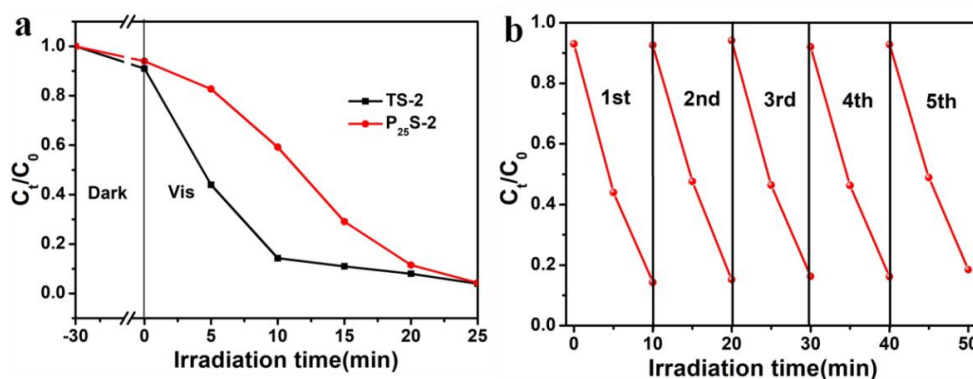


Fig. 10. (a) Photodegradation of MO over TS-2 and  $\text{P}_{25}\text{S-2}$  composites, and (b) Recycling tests of TS-2 catalyst under visible light (color online)

### 3.5. Photocatalytic mechanism

In order to study the roles various active species play during the photodegradation MO process, trapping experiments were carefully carried out using  $K_2Cr_2O_7$  as  $e^-$  scavenger, isopropyl alcohol as  $\bullet OH$  scavengers and EDTA-2Na as  $h^+$  scavenger [31]. As shown in Fig. 11, the photodegradation of MO was significantly restrained after adding  $K_2Cr_2O_7$ , indicating that the strong oxidative  $\bullet O_2^-$  radicals were the mainly active species, which generated from the dissolved oxygen reduction in water with the aid of photogenerated electrons. The relatively weak suppression effect for isopropyl alcohol is possibly related with the formed  $\bullet OH$  radicals. Meanwhile, the MO degradation was almost negligible with addition of EDTA-2Na, indicating that  $h^+$  did not participate in the photodegradation process due to the relatively lower VB potential of  $In_2S_3$ . In sum, the strong oxidative  $\bullet O_2^-$  plays a major role in organic pollutant degradation, followed by hydroxyl radicals.

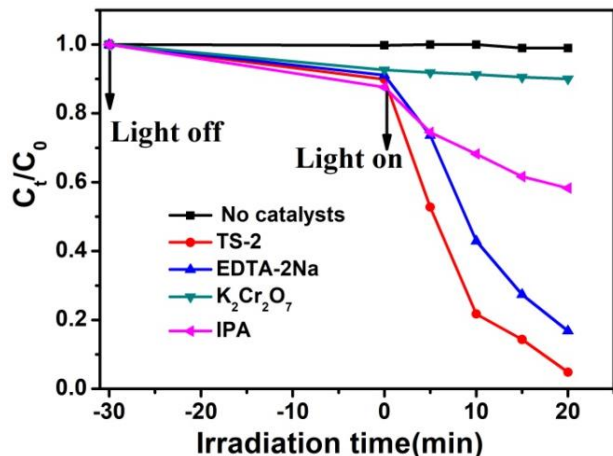


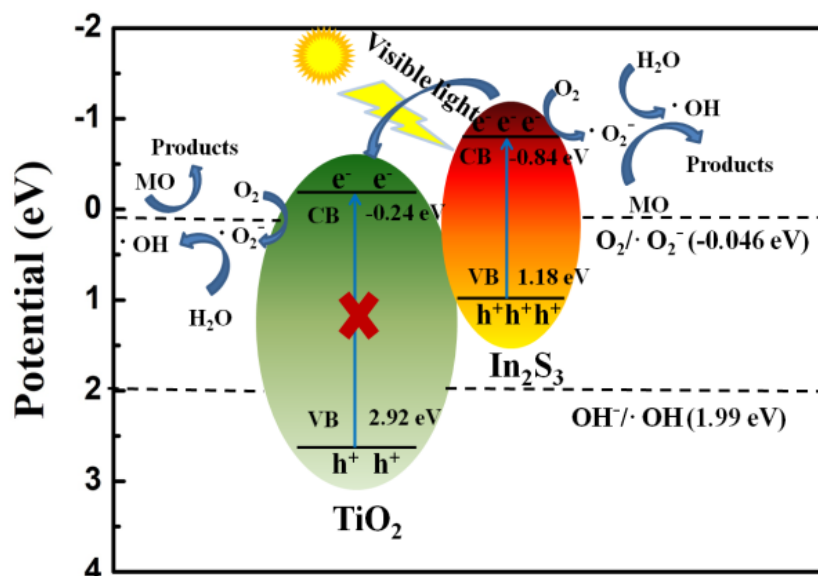
Fig. 11. Scavenger experiment on the photodegradation of MO by TS-2 under visible light irradiation (color online)

Based on the experimental analysis, it can be concluded that the broader light absorption region and higher charge separation efficiency are the main factors

for improved photocatalytic performance of  $In_2S_3/TiO_2$  heterojunction, which are determined by the band structure [46, 51]. It is believed that the band structure is composed of the band gap energy ( $E_g$ ), the valence band ( $E_{VB}$ ) energy and the conduction band ( $E_{CB}$ ) energy of materials. In order to explore the band structure in detail, the empirical equation are introduced and shown as follows [50, 52]:

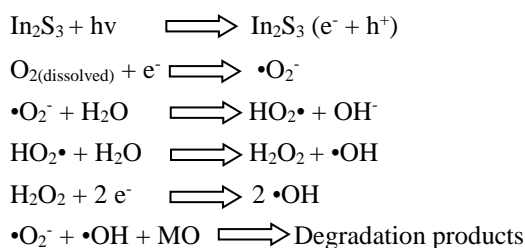
$$E_{VB} = X - E^e + 0.5E_g \quad (3)$$

where X stands for the absolute electronegativity that calculated from the geometric mean of the electronegativity of constituent atoms and  $E^e$  is the energy of free electrons refer to the hydrogen scale (ca. 4.5 eV). The X values for  $TiO_2$  and  $In_2S_3$  are counted to be 5.84 eV and 5.05 eV, respectively. Their corresponding  $E_{VB}$  of  $TiO_2$  and  $In_2S_3$  are obtained to be 2.92 eV and 1.18 eV, separately. Meanwhile the  $E_{CB}$  of them are calculated to be -0.24 and -0.84 eV, respectively. Thus, the photocatalytic mechanism for degradation of MO is tentatively proposed and schematically illustrated in Scheme 1. The  $In_2S_3$  acts as a sensitizer due to the narrow band gap energy and provides electron-hole pairs under visible light illumination. Since the  $E_{CB}$  of  $In_2S_3$  is higher than that of  $TiO_2$ , the excited electrons can migrate to the conduction band of  $TiO_2$  via the constructed heterojunction interface, which largely decreases the recombination of electron-hole pairs. Moreover, the  $O_2$  can be reduced to  $\bullet O_2^-$  by photogenerated electrons on the conduction band of  $TiO_2$  and  $In_2S_3$  due to the lower potentials than  $E_0(O_2/\bullet O_2^-)$  (0.046 eV) [53]. Besides, the partial  $\bullet O_2^-$  will transform to  $\bullet OH$  with the aid of electrons, both of which can participate in the subsequent MO degradation.



Scheme. 1 Photodegradation mechanism of In<sub>2</sub>S<sub>3</sub>/TiO<sub>2</sub> catalyst under visible light illumination (color online)

The reasonable photocatalytic degradation process of MO by In<sub>2</sub>S<sub>3</sub>/TiO<sub>2</sub> heterojunction can be clearly described as following steps:



#### 4. Conclusions

In this paper, a simple precursor-directed synthesized method was presented to construct In<sub>2</sub>S<sub>3</sub>/TiO<sub>2</sub> heterojunction with high surface area by in situ decorating TiO<sub>2</sub> nanoparticles on ultrathin In<sub>2</sub>S<sub>3</sub> nanoflakes. The morphology, structure and photoelectrochemical properties of the prepared catalyst have been investigated. The characterization results indicate that the introduction of In<sub>2</sub>S<sub>3</sub>/TiO<sub>2</sub> heterojunction design with morphology control not only broadens the light absorption region but also improves the charge separation of materials. As a result, compared with TiO<sub>2</sub>, In<sub>2</sub>S<sub>3</sub> and In<sub>2</sub>S<sub>3</sub>/P25 heterojunction, in situ constructed In<sub>2</sub>S<sub>3</sub>/TiO<sub>2</sub> heterojunction exhibits outstanding photocatalytic activity under visible light irradiation. We expect that the simple and promising strategy adopted

here would provide a rational synthesized approach for in situ fabricating heterojunction with morphology control.

#### Acknowledgements

This work was supported by the National Natural Science Foundation of China (21776059); Natural Science Foundation of Hebei Province (B2020208009); and the Five Platforms Foundation of Hebei University of Science and Technology (1182220).

#### References

- [1] E. Routoula, S. V. Patwardhan, *Environ Sci Technol* **54**, 647(2020).
- [2] T. M. Di, Q. L. Xu, W. K. Ho, H. Tang, Q. J. Xiang, J. G. Yu, *Chem. Cat. Chem.* **11**, 1394 (2019)
- [3] J. H. Li, J. Ren, Y. J. Hao, E. P. Zhou, Y. Wang, X. J. Wang, R. Su, Y. Liu, X. H. Qi, F. T. Li, *J Hazard Mater.* **401**, 123262 (2021).
- [4] H. Wu, H. L. Tan, C. Y. Toe, J. Scott, L.Z. Wang, R. Amal, Y. H. Ng, *Adv. Mater.* **32**, 1904717 (2020).
- [5] J. Yang, Y. J. Liang, K. Li, G. Yang, K. Wang, R. Xu, X. J. Xie, *Appl. Catal. B* **262**, 118252 (2020).
- [6] A. Fujishima, K. Honda, *Nature* **238**, 37 (1972).
- [7] J. Zhang, Q. Xu, Z. C. Feng, M. J. Li, C. Li, *Angew Chem. Int. Ed.* **47**, 1766 (2008).
- [8] Q. Z. Ni, J. F. Ma, C. H. Fan, Y. Kong, M. G. Peng,

- S. Komarneni, *Ceram. Int.* **44**, 19474 (2018).
- [9] D. Kim, K. K. Sakimoto, D. C. Hong, P. D. Yang, *Angew Chem. Int. Ed.* **54**, 3259 (2015).
- [10] N. Sakai, T. Tatsuma, *Adv. Mater.* **22**, 3185 (2010).
- [11] N. Wei, H. Z. Cui, C. M. Wang, G. S. Zhang, Q. Song, W. X. Sun, X. J. Song, M. Y. Sun, J. Tian, *J. Am. Ceram. Soc.* **100**, 1339 (2017).
- [12] J. K. Zhang, Z. B. Yu, Z. Gao, H. B. Ge, S. C. Zhao, C. Q. Chen, S. Chen, X. L. Tong, M. H. Wang, Z. F. Zheng, Y. Qin, *Angew Chem. Int. Ed.* **56**, 816 (2017).
- [13] Y. Wang, X. H. Liu, Q. K. Wang, M. Quick, S. A. Kovalenko, Q. Y. Chen, N. Koch, N. Pinna, *Angew Chem. Int. Ed.* **59**, 7748 (2020).
- [14] S. Jafari, M. R. Mohammadi, H. R. M. Hosseini, *Ind. Eng. Chem. Res.* **55**, 12205 (2016).
- [15] J. K. Cao, X. Z. Song, X. L. Kang, Z. D. Dai, Z. Q. Tan, *Adv. Powder Technol.* **29**, 1925 (2018).
- [16] X. M. Zhou, N. Liu, P. Schmuki, *ACS Catal.* **7**, 3210 (2017).
- [17] X. B. Chen, L. Liu, P. Y. Yu, S. S. Mao, *Science* **331**, 746 (2011).
- [18] P. Niu, T. T. Wu, L. Wen, J. Tan, Y. Q. Yang, S. J. Zheng, Y. Liang, F. Li, J. T. S. Irvine, G. Liu, X. L. Ma, H. M. Cheng, *Adv. Mater.* **30**, 1705999 (2018).
- [19] X. L. Kang, Y. Han, X. Z. Song, Tan Z. Q. Tan, *Appl. Surf. Sci.* **434**, 725 (2018).
- [20] Y. L. Chen, X. X. Cao, B. F. Gao, B. Z. Lin, *Mater. Lett.* **94**, 154 (2013).
- [21] X. Wang, X. T. Yuan, D. Wang, W. J. Dong, C. L. Dong, Y. J. Zhang, T. Q. Lin, F. Q. Huang, *ACS Appl. Energy Mater.* **1**, 876 (2018).
- [22] H. Song, C. X. Li, Z. R. Lou, Z. Z. Ye, Zhu L. P. Zhu, *ACS Sustain. Chem. Eng.* **5**, 8982 (2017).
- [23] N. X. Li, X. Y. Zou, M. Liu, L. F. Wei, *J. Phys. Chem. C* **121**, 25795 (2017).
- [24] X. J. Wang, W. Y. Yang, F. T. Li, J. Zhao, R. H. Liu, S. J. Liu, B. Li, *J. Hazard Mater.* **292**, 126 (2015).
- [25] M. M. Han, L. M. Yu, W. Y. Chen, W. Z. Wang, J. H. Jia, *Appl. Surf. Sci.* **369**, 108 (2016).
- [26] Y. H. Yu, F. H. Chen, L. Ye, H. Zhou, T. Zhao, *J. Mater. Sci.* **54**, 10191 (2019).
- [27] Y. Y. Zhang, H. W. Hu, W. W. Kang, G. J. Qiu, R. Y. Liang, L. F. Deng, H. R. Yuan, *Ceram. Int.* **46**, 17606 (2020).
- [28] B. Chai, T. Y. Peng, P. Zeng, J. Mao, *J. Mater. Chem.* **21**, 14587 (2011).
- [29] Q. Q. Hu, G. W. Chen, Y. Q. Wang, J. C. Jin, M. T. Hao, J. R. Li, X. Y. Huang, *J. Jiang, Nanoscale* **12**, 12336 (2020).
- [30] F. L. Wang, Z. M. Jin, Y. J. Jiang, E. H. G. Backus, M. Bonn, S. N. Lou, D. Turchinovich, R. Amal, *Appl. Catal. B* **198**, 25 (2016).
- [31] J. Park, T. H. Lee, C. Kim, S. A. Lee, H. Kim, J. W. Yang, J. Lim, H. W. Jang, *Appl. Catal. B* **295**, 120276 (2021).
- [32] D. M. Ma, W. Y. Liu, Q. Chen, Z. Jin, Y. Zhang, J. Huang, H. Zhang, F. M. Peng, T. Luo, *J. Solid State Chem.* **293**, 121791 (2021).
- [33] X. Zhang, X. H. Li, C. L. Shao, J. H. Li, M. Y. Zhang, P. Zhang, K. X. Wang, N. Lu, Y. C. Liu, *J. Hazard Mater.* **260**, 892 (2013).
- [34] C. Gao, J. T. Li, Z. C. Shan, F. Q. Huang, H. L. Shen, *Mater. Chem. Phys.* **122**, 183 (2010).
- [35] B. Chai, Peng T. Y. Peng, P. Zeng, J. Mao, *J. Mater. Chem.* **21**, 14587 (2011).
- [36] X. Y. Wang, H. X. Li, J. Zhang, X. G. Liu, X. F. Zhang, *J. Alloys Compd.* **831**, 154798 (2020).
- [37] H. B. Yao, X. Zhang, X. H. Wang, S. H. Yu, J. Li, *Dalton Trans.* **40**, 3191 (2011).
- [38] Y. Bai, I. Mora-Seró, F. D. Angelis, J. Bisquert, P. Wang, *Chem. Rev.* **114**, 10095 (2014).
- [39] J. Zhao, Y. P. Liu, M. H. Fan, L. Yuan, X. X. Zou, *Inorg. Chem. Front.* **2**, 198 (2015).
- [40] J. Zhao, X. X. Zou, J. Su, P. P. Wang, L. J. Zhou, G. D. Li, *Dalton Trans.* **42**, 4365 (2013).
- [41] N. Q. Wu, J. Wang, D. N. Tafen, H. Wang, J. G. Zheng, J. P. Lewis, X. G. Liu, S. S. Leonard, A. Manivannan, *J. Am. Chem. Soc.* **132**, 6679 (2010).
- [42] W. W. Gao, W. X. Liu, Y. H. Leng, X. W. Wang, X. Q. Wang, B. Hu, D. H. Yu, Y. H. Sang, H. Liu, *Appl. Catal. B* **176**, 83 (2015).
- [43] X. Tian, Y. J. Sun, J. Y. He, X. J. Wang, J. Zhao, S. Z. Qiao, F. T. Li, *J. Mater. Chem. A* **7**, 7628 (2019).

- [44] W. Ren, J. J. Cheng, H. H. Ou, C. J. Huang, M. M. Titirici, X. C. Wang, *Chem. Sus. Chem.* **12**, 3257 (2019).
- [45] J. M. Cai, Y. T. Wang, Y. M. Zhu, M. Q. Wu, H. Zhang, X. G. Li, Z. Jiang, M. Meng, *ACS Appl. Mater. Interfaces* **7**, 24987 (2015).
- [46] H. Wang, X. Z. Yuan, Wu Y. Wu, G. M. Zeng, H. R. Dong, X. H. Chen, L. J. Leng, Z. B. Wu, L. J. Peng, *Appl. Catal. B* **186**, 19 (2016).
- [47] X. J. Wang, X. Tian, F. T. Li, J. Zhao, Y. P. Li, R. H. Liu, Y. J. Hao, *Dalton Trans.* **44**, 17859 (2015).
- [48] H. L. Tan, F. F. Abdi, Y. H. Ng, *Chem. Soc. Rev.* **48**, 1255 (2019).
- [49] X. W. Wang, W. X. Liu, X. Q. Wang, D. H. Yu, H. Liu, *Sci. Adv. Mater.* **7**, 479 (2015).
- [50] M. Q. Yang, B. Weng, Y. J. Xu, *Langmuir* **29**, 10549 (2013).
- [51] J. G. Guo, Y. Liu, Y. J. Hao, Y. L. Li, X. J. Wang, R. H. Liu, F. T. Li, *Appl. Catal. B* **224**, 841 (2018).
- [52] J. Cao, B. D. Luo, H. L. Lin, B. Y. Xu, S. F. Chen, *Appl. Catal. B* **111**, 288 (2012).
- [53] Y. Zuo, J. J. Chen, H. C. Yang, M. Zhang, Y. F. Wang, G. He, Z. Q. Sun, *J. Mater Chem C* **7**, 9065 (2019).

---

\*Corresponding author: xiaojun.5707406@163.com;  
yqcheng@hbu.edu.cn